Resonant soft x-ray inelastic scattering and soft x-ray emission study of the electronic structure of α-MoO_3

T. Learmonth,[1] C. McGuinness,[2] P.-A. Glans,[1] B. Kennedy,[2] J. St. John,[1] J.-H. Guo,[3] M. Greenblatt,[4] and K. E. Smith[1,*]

[1]*Department of Physics, Boston University, 590 Commonwealth Avenue, Boston, Massachusetts 02215, USA*

[2]*School of Physics, Trinity College Dublin, Dublin 2, Ireland*

[3]*Advanced Light Source, Lawrence Berkeley National Laboratory, Berkeley, California 94720, USA*

[4]*Department of Chemistry and Chemical Biology, Rutgers University, 610 Taylor Road, Piscataway, New Jersey 08854, USA*

(Received 2 June 2008; revised manuscript received 25 October 2008; published 13 January 2009)

The electronic structure of quasi-low-dimensional solids is a topic of enduring interest due to the complex many-body interactions that exist in such materials and their resulting exotic physical properties. A well studied class of such materials is the quasi-low-dimensional metals known collectively as molybdenum oxide bronzes. These materials are all derived from the band insulator α-MoO_3. We report here a study of the electronic structure of α-MoO_3 using resonant inelastic x-ray scattering and soft x-ray emission spectroscopy. We observe significant variation in x-ray scattering as a function of the relative orientation of the polarization vector of the incident light and the crystal axes. We interpret our data using a model of **k**-selective soft x-ray scattering.

DOI: 10.1103/PhysRevB.79.035110 PACS number(s): 78.70.En

I. INTRODUCTION

The electronic structure of quasi-low-dimensional solids is a topic of enduring interest due to the complex many-body interactions that exist in such materials and their resulting exotic physical properties. While many quasi-low-dimensional *metals* have been studied extensively using angle-resolved photoemission spectroscopy (ARPES),[1] similar studies of the electronic structure of quasi-low-dimensional *insulators* are more limited due to charging problems associated with photoemission from nonconducting samples. Since many quasi-low-dimensional conductors are chemically derived from parent insulating materials, knowledge of the electronic structure of such insulators is highly desirable to form a comprehensive picture of these systems. A case in point is the well studied class of quasi-low-dimensional metals known collectively as molybdenum oxide bronzes. These materials are all derived from the band insulator α-MoO_3, which has a band gap of approximately 3 eV.[2,3] While the electronic structure of $K_{0.3}MoO_3$, $Li_{0.9}Mo_6O_{17}$, and $Na_{0.9}Mo_6O_{17}$ have been extensively studied,[4] the same cannot be said for insulating α-MoO_3.

We report here a study of the electronic structure of α-MoO_3 using resonant inelastic x-ray scattering and soft x-ray emission spectroscopy. These are complementary probes to photoemission spectroscopy in the study of electronic structure in solids, and since they are photon in/photon out spectroscopies, they are unaffected by sample charging. Soft x-ray emission spectroscopy (XES) involves the measurement of the photon emitted when an electron from the valence band makes a direct radiative transition into a hole on a localized core level; the hole is created by excitation of a core electron with monochromatic synchrotron radiation. Since strong dipole selection rules govern the radiative transition to the core hole, XES directly measures the orbital angular-momentum resolved partial density of states (PDOS).[5] Furthermore, since the core level is associated with a specific element in a compound, it is the element specific PDOS that is measured. In the case of inequivalent lattice sites of a given element, a core hole on a specific site may be preferentially selected due to considerations of excitation energy selectivity or polarization selectivity; in such a case XES measures the angular-momentum resolved PDOS localized to that site. Additional information can be extracted from emission spectra if the energy of the incident monochromatic synchrotron radiation is tuned close to a core-level absorption threshold. In this resonant case, the system is not ionized, and the excited core electron resides in the conduction band. Emission features can appear that are associated with excitations near E_F; i.e., the incident photon, resonant with a core level, excites an electron-hole pair around E_F and scatters from the system with an energy shifted to lower values by the characteristic energy of the valence excitation. This variant of XES is known as resonant inelastic x-ray scattering (RIXS).[6] RIXS spectral features are energy losses from the main excitation energy, and thus such features change their (emission) energy with changes in the incident photon energy. This is in contrast to PDOS emission features seen in XES, which are fixed at the energy associated with the transition into the core hole. This makes the identification of PDOS and RIXS features in XES spectra straightforward. RIXS features can also be **k** selective in certain solids, as will be discussed below.[7–9] The manner in which **k**-selective RIXS samples the Brillouin zone allows for exploitation of the alignment in **k** space of axes of strong and weak dispersions above and below the Fermi level (E_F). In this way one can potentially exploit the lack of dispersion along one or more axes that is characteristic of low dimensional materials. We have observed significant variation in x-ray scattering from α-MoO_3 as a function of the relative orientation of the polarization vector of the incident light and the crystal axes. We interpret our data using a model of **k**-selective soft x-ray scattering while also taking into account the contributions of the various inequivalent atomic sites to the participating bands. This allows a comprehensive study of the electronic structure of α-MoO_3.

The crystal structure of α-MoO_3 consists of chains of MoO_6 octahedra as the basic building blocks.[10,11] The octa-

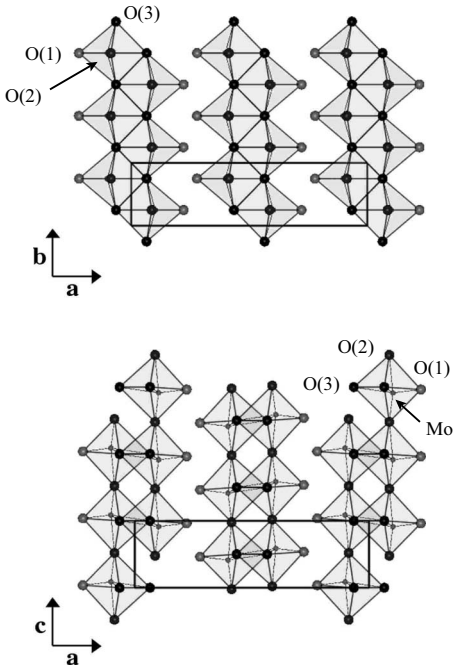

FIG. 1. The crystal structure of α-MoO_3, looking down on the **a**-**b** plane. Top panel: view with the chains of octahedra along the vertical **b** axis, and looking down on the **a**-**c** plane; bottom panel: view with the chains of octahedra sharing corners along the vertical **c** axis. The three O sites and single Mo site are marked on the figure. The convention of Rozzi *et al.* (Ref. 13) is used in labeling the O sites. The unit cell is displayed as a thick line in both panels. The *Pnma* space group is used. The alternate space-group *Pbnm* can also be used to compare *Pnma* to *Pbnm*: **a**→**b**, **b**→**c**, and **c**→**a**.

hedra are strongly bonded along **b** and **c** axes but only weakly along the **a** axis, and the crystal structure can be viewed as zigzag chains of edge sharing MoO_6 octahedra along the **b** axis that are connected by corner O sites to adjacent chains forming infinite layers in the **b**-**c** plane (see Fig. 1). Here we use the *Pnma* space group but the equivalent *Pbmn* space group, which serves to rotate the crystal axis labels, is also used in some of the studies referenced.[12,13] The octahedra are not symmetric, with two legs significantly longer than the other four due to a Jahn-Teller type distortion.[11] This has sometimes led the α-MoO_3 structure to be considered in terms of tetrahedra rather than octahedra. There are three inequivalent O sites: O(1) bonds to only one Mo site on the outside edge of each double chain, O(2) sites join two Mo sites along the **b** axis, and O(3) sites bond to two Mo sites in between chains along the **c** axis, with a third Mo-O(3) bond along the **a** axis.[13–15] From an electronic structure perspective, each MoO_6 octahedron can be treated to first approximation without considering any interaction between octahedra.[3] In this case the resulting molecular orbitals will broaden into bands in the solid. This approach yields a starting point of the basic features of the electronic structure of α-MoO_3. Without considering the effects of the distortion of the octahedra, the Mo $4d(t_{2g})$ orbitals hybridize with the O $2p(\pi)$ orbitals to form relatively narrow π and π^* bands. Further from E_F, Mo $4d(e_g)$ orbitals mix with O $sp(\sigma)$ orbitals to form broad σ and σ^* bands. Finally there is also a narrow O $2p$ nonbonding band at the top of the valence band nearest E_F. Thus the band gap lies between the O $2p$ nonbonding band and the π^* band. Since the π^* states have some metal d character, optical transitions across the gap are dipole allowed and such measurements indicate that the gap is approximately 3 eV in magnitude.[2,3] This starting point allows convenient comparison with numerical calculations of the electronic structure of α-MoO_3.[13–15]

II. EXPERIMENT

XES, RIXS, and soft x-ray absorption spectroscopy (XAS) measurements were made at the O K edge of α-MoO_3. Experiments were undertaken at beamline 7.0.1 at the Advanced Light Source (ALS), Lawrence Berkeley National Laboratory, and at beamline I511–3 at MAXLab in Lund, Sweden. Both beamlines are equipped with soft x-ray undulators with fixed linear polarization. However the MAX-laboratory endstation at I511–3 allows the x-ray emission/scattering spectrometer to be rotated outside of the plane of polarization defined by the incident photon polarization vector and the Poynting vector; the ALS endstation has its spectrometer fixed inside the polarization plane. In both cases the x-ray emission spectrometer is at 90° to the direction of the incident beam. XAS measurements were made using a silicon diode to measure total fluorescence yield. XES and RIXS measurements were made using a Nordgren-type Rowland circle x-ray emission spectrometer.[16] Needle-like single crystals of α-MoO_3 were cleaved in air along the **b**-**c** plane before introduction to the experimental endstations, both of which maintain a base pressure of 1×10^{-9} Torr. The XAS data presented here were collected with an energy resolution of 0.2 eV. The XES and RIXS data were collected with an incident photon energy resolution of 0.5 eV and a spectrometer energy resolution of 0.4 eV. All measurements were made at room temperature. The beamline energy was calibrated at the ALS using the O K-edge x-ray absorption structure of NiO.[17] At both endstations the O K-edge emission was calibrated to metallic Zn $L_{\alpha 1,2}$ and $L_{\beta 1}$ emission lines in second order. In an idealized experiment, the crystal axes can be rotated with respect to the polarization vector of the incident x rays in order to measure in absorption the axis-resolved PDOS of the conduction band. Then for each crystal orientation, the emission spectrometer could be moved to detect radiation emitted from each pair of crystal axes which are perpendicular to the line of sight, giving a linear combination of the occupied PDOS of the valence band projected along these axes. In reality, there are limitations to the geometries that can be probed. Figure 2 presents an illustration of the geometries that were accessible to us in this experiment, along with the axes orbital projections that are approximately probed in the absorption and emission process for each geometry. Of necessity, the experimental geometry departs from the ideal by the angular amount indicated in Fig. 2. This can lead to both a modification of the states selected (in proportion to the square of the sine of the angular deviation from the exact geometry) and a modification of intensity of emission fea-

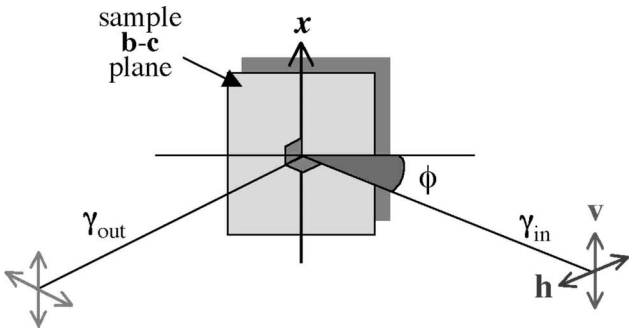

Panel Label	Actual Geometry			Approx. Geometry	
	polarization	*x* axis	ϕ	E_{in}	E_{out}
A	h	**c**	15°	**a**	**b, c**
B	h	**c**	75°	**b**	**a, c**
C	v	**b**	15°	**b**	**b, c**
D	h	**b**	75°	**c**	**a, b**
E	v	**c**	75°	**c**	**a, c**

FIG. 2. Illustration of the experimental geometry. The incident photon is polarized either vertically (v) or horizontally (h), and makes an angle ϕ with the sample **b**-**c** surface plane. The orientation of the sample is given by the ***x*** axis assignment. The emission spectrometer is positioned at 90° to the incident photon beam, and either perpendicular (v) or parallel (h) to the incident photon polarization vector. The sample is mounted on a manipulator that allows rotation about the ***x*** axis to set the angle ϕ. The RIXS data in Fig. 4 are presented in panels labeled A–E. For each panel, the experimental geometries are listed here, along with the approximate α-MoO_3 crystal axes that are parallel to the incident ($\mathbf{E}_{in}$) and detected ($\mathbf{E}_{out}$) photon polarization vectors. The geometry uses the approximation $\sin(75°) \approx 1$ and $\sin(15°) \approx 0$, and as such is only presented for visualization purposes.

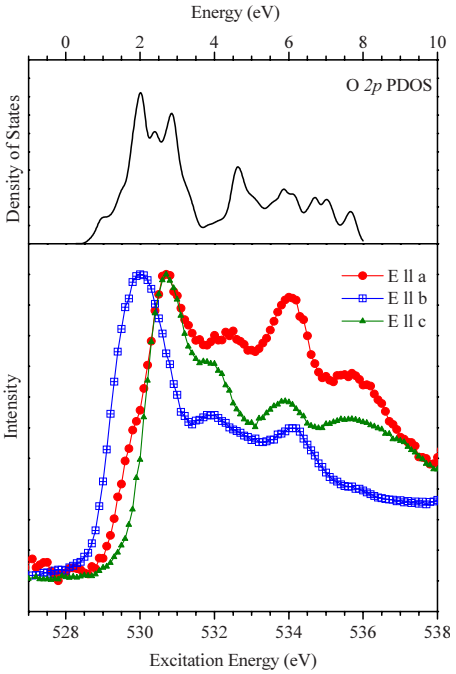

FIG. 3. (Color online) The top panel shows the combined O 2*p* PDOS as published by Rozzi *et al.* (Ref. 13). The bottom panel shows the O *K*-edge XAS spectra collected with the incident photon polarization vector approximately aligned to each α-MoO_3 crystal axis, corresponding to geometries A, B, and D listed in Fig. 2.

tures with specific angular dependence (again in proportion to the angular deviation of the direction of the emission from the stated crystal axis).

III. RESULTS

Figure 3 presents three O *K*-edge XAS spectra recorded with the polarization vector of the incident light parallel to each of the α-MoO_3 crystal axes. Also shown in Fig. 3 is the calculated O 2*p* PDOS projected along each crystal axis as published by Rozzi *et al.*,[13] which is broadly similar to other calculations.[14,15] The XAS results are in good agreement with previously published spectra.[12] The calculated O 2*p* PDOS has been broadened with a 200 meV Gaussian function to simulate the experimental broadening of the experiment. Lifetime broadening is not included as this simple comparison with the unoccupied PDOS is intended as a guide for our discussion. To aid the comparison of the measured XAS spectra and the calculated PDOS, a rigid shift of 528 eV has been applied to the calculations to align the conduction-band minimum with the measured absorption onset. Along all three axes, there is a 2 eV wide cluster of states just above conduction-band minimum, and a 3–4 eV wide band following a minimum in the PDOS. Comparing to the molecular model and previous experiments, these bands correspond to the expected π^* and σ^* bands, respectively.[3,13,18] At the O *K* edge, there are no multiplet effects in the XAS spectrum so a direct comparison with the calculated PDOS is meaningful, and indeed there is qualitative agreement between the calculated PDOS and the XAS spectra.[19] Note that the π^* peak resides at lower energy in the $\mathbf{E}_{in} \| \mathbf{b}$ spectrum, with much smaller but detectable weight in the $\mathbf{E}_{in} \| \mathbf{a}$ spectrum. The lowest energy unoccupied band is thus most strongly accessed for RIXS in the $\mathbf{E}_{in} \| \mathbf{b}$ orientation. Furthermore, this π^* band as observed in O *K*-edge XAS is dominated by contributions from O(1) and O(2) with little contribution from O(3) in the lower part of this energy region, i.e., at the O *K*-edge threshold.[13,15]

Figures 4–6 show five sets of O *K*-edge RIXS spectra taken with different experimental geometries along with their respective XAS spectra. The RIXS excitation energies are marked on each XAS spectrum. Figure 2 lists the experimental geometry of each of the RIXS panels along with the incident and detected polarizations. The most striking results are those in geometry B, shown in Fig. 5. Spectra *a*–*d* are dominated by two main features, which we will refer to as *i* and *ii*, at 524.5 and 525.9 eV, respectively. As compared to the above threshold, XES fluorescencelike spectrum *g*, these two features are also accompanied by a reduction in spectral weight everywhere else but most especially at emission energies higher than feature *ii*. As the excitation energy is increased from spectrum *a* to spectrum *d*, feature *i* moves slowly toward higher emission energy by approximately 0.3 eV before fading completely. Feature *ii* moves less, by ap-

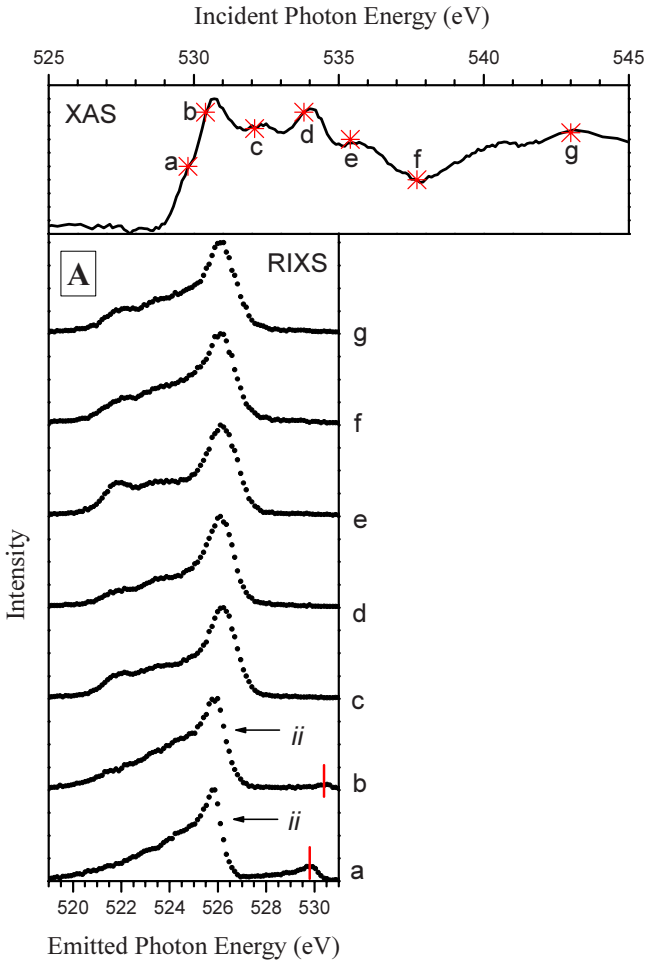

FIG. 4. (Color online) RIXS spectra from α-MoO_3 in experimental geometry A. The top panel shows the XAS spectrum corresponding to the RIXS spectra in the bottom panel with the RIXS excitation energies marked. Feature *ii* is explained in the text. The excitation energy for each spectrum is marked with a vertical bar, which coincides with the elastic feature when present. The experimental geometry is illustrated in Fig. 2.

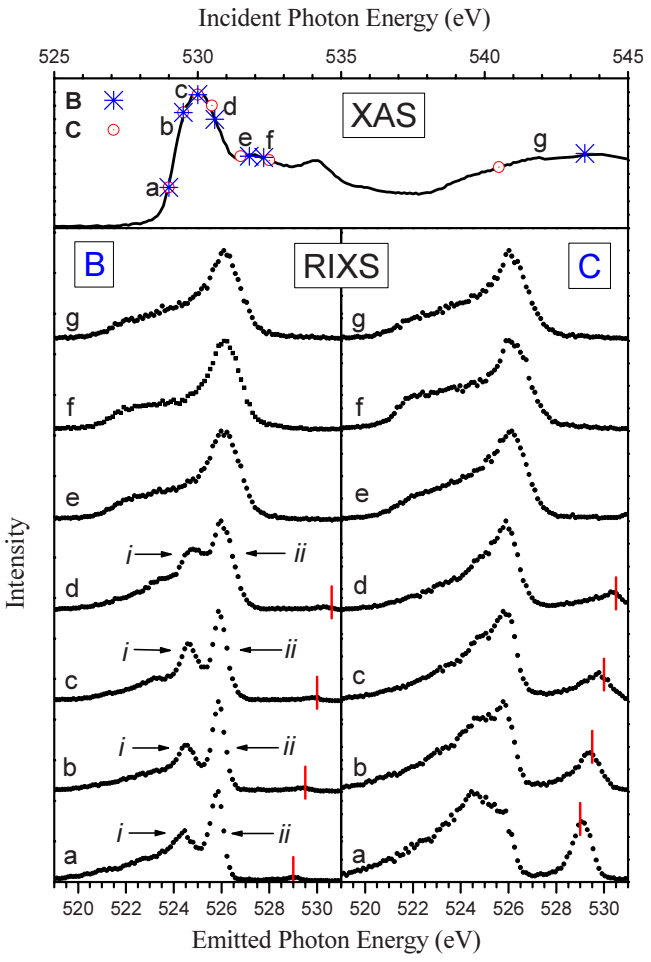

FIG. 5. (Color online) RIXS spectra from α-MoO_3 in experimental geometries B and C. The top panel shows the XAS spectrum corresponding to the RIXS spectra in the bottom panel with the RIXS excitation energies marked. Features *i* and *ii* are explained in the text. The excitation energy for each spectrum is marked with a vertical bar, which coincides with the elastic feature when present. The experimental geometry is illustrated in Fig. 2.

proximately 0.1 eV over the same excitation energies.

In geometry A (Fig. 4), spectra *a* and *b* are quite similar to the lower excitation energy geometry B, with the exception of feature *i*. There is a strong reduction in spectral weight below 523 eV, which corresponds to the σ states in the valence band,[18] and at emission energies higher than feature *ii*. The strong intensity of the RIXS features in geometries A and B is noteworthy.

In geometries C–E, there are two features similar to features *i* and *ii* although they display much weaker spectral intensity than in geometries A and B. They are less prominent perhaps due to increased width or also because of the different experimental geometry. In all three geometries (C–E), we observe two features moving in emission energy with changing excitation energy. These features are accompanied by the suppression of σ derived spectral weight below 523 eV. Figure 7 shows the energy dependence of all the spectral features analogous to *i* and *ii* observed in each orientation measured. We observe two features in all geometries with the exception of geometry A. The higher energy feature in each case is near 526 eV, and moves slowly in emission energy over the range of excitation energies for which it is observed. The lower energy feature, nearer to 525 eV, moves in emission energy more quickly over the same excitation energy range.

There is a fundamental difference between the RIXS features measured in geometries C and E, and geometries A, B, and D. In geometries A, B, and D the polarization vector of the incident x-rays is orthogonal to the polarization of the detected x rays. As a result, the elastic-scattering process, where the RIXS final state is the ground state, is suppressed. This is in contrast to geometries C and E, where the incident x-ray polarization vector is parallel to a component of the detected x-ray polarization vectors. Strong elastic spectral features are visible in geometries C and E, and weak elastic features are visible at low RIXS excitation energies in geometries A, B, and D. These features are marked with a vertical bar in each of Figs. 4–6.

Lastly, it is instructive to compare the RIXS spectra recorded with the lowest excitation energies in each geometry,

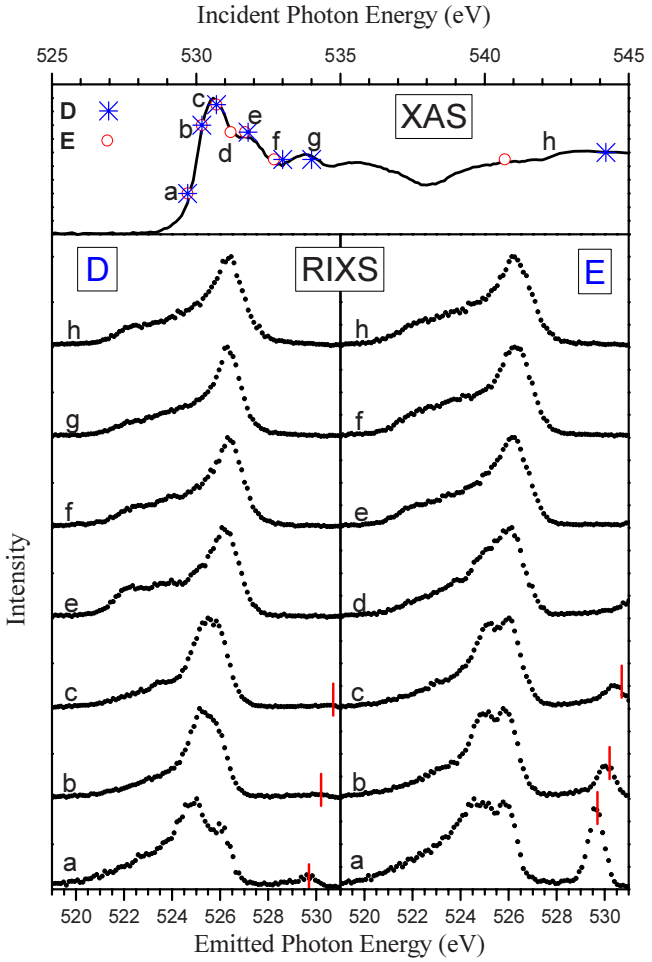

FIG. 6. (Color online) RIXS spectra from α-MoO_3 in experimental geometries D and E. The top panel shows the XAS spectrum corresponding to the RIXS spectra in the bottom panel with the RIXS excitation energies marked. The excitation energy for each spectrum is marked with a vertical bar, which coincides with the elastic feature when present. The experimental geometry is illustrated in Fig. 2.

with the XES spectra recorded using excitation energies far above threshold. This comparison is presented in Fig. 8. The above-threshold spectra are not **k** selective and sample all oxygen sites equally, leading to a rather similar spectrum in each case even though the spectrum from each geometry should be a summation of two axis projected oxygen 2*p* PDOS as selected by the measurement geometry (see Fig. 2). The RIXS spectra clearly show that in geometries D and E the observed maximum emission energy is shifted to ~527 eV from about 526.5 eV for geometries A, B, and C.

IV. DISCUSSION

The behavior of the loss feature *i* in spectra *a*–*d* in Fig. 5, with a shift in emission energy with excitation energy and the suppression of the total fluorescencelike weight, is indicative of momentum selection in RIXS.[7,8] The XAS spectrum in Fig. 5 reveals that these emission spectra result from the excitation of a core electron into a single π^* feature in the

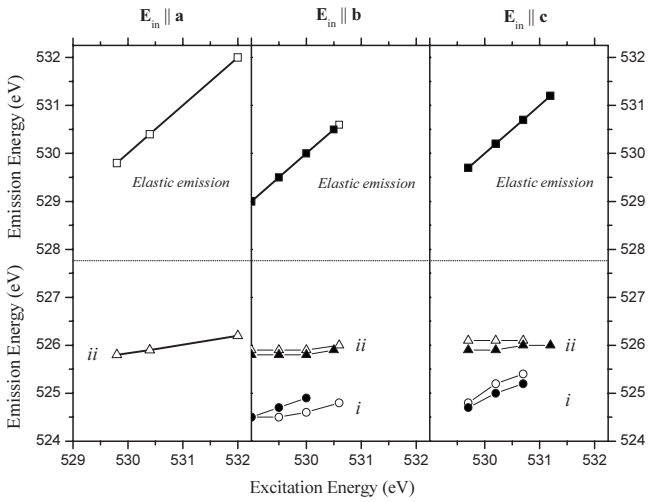

FIG. 7. The emission energies of the RIXS features in Figs. 4–6 plotted against their corresponding excitation energies. The three columnar panels represent the three incident photon polarizations: the $E_{in}\|\mathbf{a}$ panel presents the data from Fig. 4, the $E_{in}\|\mathbf{b}$ panel presents the data from Fig. 5 (geometry B=open symbol and C =closed symbol), and the $E_{in}\|\mathbf{c}$ panel presents the data from Fig. 6 (geometry D=open symbol and E=closed symbol). The top half of each panel shows the excitation energies, and the bottom half shows the corresponding emission energies of the RIXS features.

XAS spectrum. In momentum selective RIXS, this empty state must display significant dispersion. Band structure calculations show that the minimum of this band occurs at the bulk Brillouin-zone center (Γ) and that the band disperses

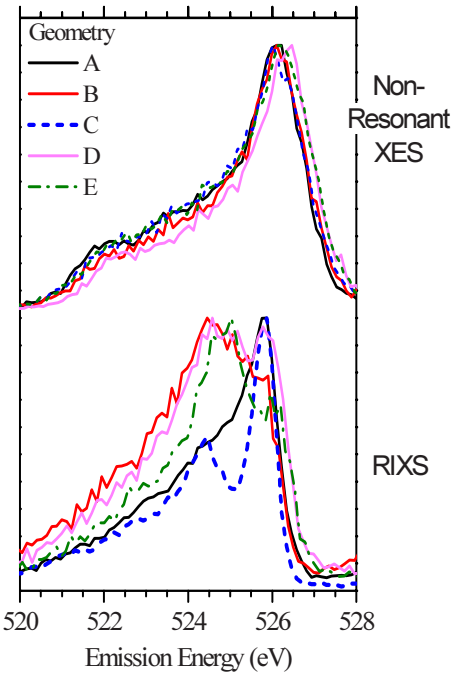

FIG. 8. (Color online) Comparison of the above-threshold nonresonant XES spectra recorded in each geometry (excitation energy "*g*" in the XAS spectra of Figs. 4–6) and the corresponding lowest energy RIXS spectra (excitation energy "*a*" in the XAS spectra of Figs. 4–6).

over the width of the XAS feature, which is approximately 2 eV.[14,15] When one measures RIXS with this incident polarization orientation, the lowest excitation energy excites electrons into states nearest to the Γ point, and due to **k** conservation, the emission process favors occupied states of the same momentum.[8,9] Thus in spectrum *a*, features *i* and *ii* are due to emission from two occupied bands near the symmetry point selected in the absorption process. As noted previously the core holes are created principally on the O(1) and O(2) sites in this configuration.[13,15] As a result not every band with oxygen character at this symmetry point can be expected to contribute to the observed oxygen RIXS spectrum. As the excitation energy increases, the **k** points probed follow the dispersion of the unoccupied band away from the Γ point. Thus the elastic feature visible in spectra *a*–*d* is associated with an unoccupied band moving toward the Brillouin-zone boundary. Features *i* and *ii* represent emission from occupied states of definite **k** at the same **k** points, which could be in principle compared to band-structure calculations. A plot of both the unoccupied and occupied band structures has been published by Sayede *et al.*[15] Comparison with this is difficult as this set of high-symmetry paths through the zone cannot give the whole picture since with increasing energy the excitation moves away from the zone center along multiple directions simultaneously. The RIXS process samples an ever increasing set of **k** points along both Γ-*Y* and lines parallel to Γ-*Y*, and Γ-*Z* and lines parallel to Γ-*Z*. The conduction-band dispersion is significantly greater along the Γ-*Z* direction but the valence dispersion is also greater along Γ-*Z*.[14,15] Thus even though the steps in **k** are largest along $\mathbf{k}_y$ as the excitation energy is increased from threshold, the smaller steps along $\mathbf{k}_z$ are associated with faster changes in the valence band. This makes it difficult to separate spectral changes due to the progression in **k** space along $\mathbf{k}_y$ from those due to the progression along $\mathbf{k}_z$.

As mentioned earlier, a further complexity in the study of α-MoO_3 using RIXS is the presence of a number of inequivalent oxygen sites. However, the emission in geometry B measured while exciting above threshold should comprise that of the oxygen 2*p* partial density of states projected along both the **a** and **c** axes, and this does in fact compare well with the published DFT calculations.[13,15] At threshold, we see only a subset of this as we are selecting specific **k** points and specific proportions of core holes on differing oxygen sites, as well as projecting only the components of the oxygen 2*p* orbitals parallel to either **a** or **c** on these sites and at these **k** points.

Given that the same intermediate states are accessed in geometries B and C, **k**-selective RIXS features in geometry C can be expected. Weak **k**-selective features are indeed visible in the C geometry of Fig. 5. The difference in the prominence of the features in this geometry compared to those previously described is quite large. The origin of the difference lies in the nature of the final state. It is important to note that the suppression of spectral weight at low emission energies is comparable in both geometries B and C, indicating that the conditions of **k** selectivity are comparable. The states responsible for these features appear only weakly accessed in geometry C but the other emission features that contribute to the fluorescence spectra are still suppressed due to **k** selectivity. The essential difference in the final state between geometry B which is lacking in geometry C is the component of the orbital projection along the **a** axis for the same selected **k** points (see Fig. 2). It is thus tempting to assign features *i* and *ii* in geometry B exclusively to the projection of these selected states along the **a** axis. Note that there is little or no dispersion of bands along the Γ-*X* direction (or along parallel directions) due to lack of hybridization of the Mo ($4d_{xz}$) orbitals,[14,15] giving rise to these dispersionless bands and hence sharp spectral features. In addition, keeping in mind that O(3) is only weakly accessed, the projected local PDOS parallel to **a** for O(1) and O(2) from these calculations gives sharp peaks at approximately these energies. The shift in energy position of these features, as **k** points further from the zone center are selected, reflects the dispersion in energy along Γ-*Y* and Γ-*Z* since the projected states along Γ-*X* at the center, proceeding to *Y*-*S* at the boundary are essentially dispersionless.[15]

The situation is more complicated with geometries D and E since the intermediate states are different from the ones accessed in geometries B and C. The O *K*-edge absorption onset for $\mathbf{E_{in}} \| \mathbf{c}$ is significantly higher in geometries D and E (Fig. 6) than in geometries B and C (Fig. 5). This higher XAS onset means that the lowest excitation energy RIXS spectrum ("*a*") in Fig. 6 is associated with states that are already above the region in **k** space where the strongest RIXS features were observed in geometry B. As mentioned earlier, the $\mathbf{E_{in}} \| \mathbf{c}$ geometry does not appear in XAS to access the same low energy unoccupied band present in the other XAS orientations (see Fig. 3), and as such in geometries D and E we cannot separate the effects of the intermediate state from those of the final state.

In geometry A (Fig. 4), the low energy XAS feature accessed in the $\mathbf{E_{in}} \| \mathbf{b}$ orientation is only weakly visible. In this geometry it was only possible to collect two RIXS spectra with excitation energies corresponding to the lowest energy feature due to resolution and signal strength constraints. Spectra *a* and *b* look quite similar, especially in the strength of the main feature, to the equivalent spectra in geometry B with the exception of the lack of feature *i*. In geometry A the features in spectra *a* and *b* are equally well defined as in geometry B. However, not only is there no sign of a feature *i*, there is no reduction in spectral weight (as compared to higher excitation energies) at emission energies corresponding in between features *i* and *ii*. This is perhaps an indication that the band corresponding to this feature is represented in spectra *a* and *b* but without **k** selectivity along an axis of large dispersion. In the other geometries, we observe the lower energy feature dispersing toward E_F as **k** increases from Γ. Thus at the lowest excitation energies, when **k** selectivity is present, only the lowest energy states in the band contribute to the observed spectrum. With positive dispersion, if there is no **k** selectivity along the direction in the Brillouin zone through which the lower energy band disperses, we would expect the band to contribute spectral weight at both the energy of the lower energy features and at higher energies, depending on the extent in energy of the band, regardless of its extent in **k** space. Thus the shift in spectral weight from the lower energy feature to higher energies is the signature of lack of **k** selectivity along a direction of strong dispersion.

The **k**-selective spectra collected in geometries A and B are particularly well resolved as compared to the other orientations. This difference entails both the narrow width of the features themselves, and strong suppression of the spectral weight away from the **k**-selective features. The feature definition is also exceptional when compared to other observations of **k**-selective RIXS. The suppression of spectral weight away from the **k**-selective features is due to the strong suppression of non **k**-selective emission. There is also the possibility that the strongly **k**-selective emission is aided by the quasilow dimensionality of α-MoO_3. Along the **a** axis in α-MoO_3, there is only weak bonding and thus only weak dispersion of bands along Γ-X near the Fermi level.[15] Thus lack of **k** selectivity along Γ-X does not lead to the broadening of otherwise **k**-selective features as it does along strongly dispersive axes. This implies that low dimensional materials may actually be a fruitful category of solids for the use of RIXS in probing band structure. Figure 7 summarizes many of our findings and it can be viewed in each case as the progression from the zone center toward the zone boundary of the projection of the **k**-selected RIXS on the crystal axes defined by the geometry. In the case of geometry B ($\mathbf{E_{in}}\|\mathbf{b}$), as the energy is increased the projection along the almost dispersionless **a** axis changes from the line Γ-X which contains the zone center until we reach the zone boundary where we then project along a parallel line near the zone boundary along Γ-Y and approximately halfway to the boundary along Γ-Z. Thus Fig. 7 demonstrates the difference in energy for the same bands at the zone center and zone boundary.

The selectivity in the RIXS spectra can clearly be demonstrated when comparing the first RIXS spectra for the different geometries as shown in Fig. 8. Here the increased spectral weight above 526.5 eV observed only in geometries D and E is principally due to the contribution to the emission spectra of oxygen states nearer E_F due to **k** points being selected far from the zone center due to the delayed absorption onset for $\mathbf{E_{in}}\|\mathbf{c}$. A similar lowest excitation energy for geometry A, while still suppressing spectral weight above 526.5 eV, reflects the weak dispersion of the occupied oxygen states selected in this geometry while the lowest energy RIXS spectra in B and C select the more strongly dispersing states.

We have not addressed the effect on **k**-selective RIXS of the exciton created by the core hole in the intermediate RIXS state. The effect of the core hole was studied in graphite, which exhibits strongly excitonic behavior.[20] The effect on the RIXS results are not entirely in agreement in these studies but it is clear that XAS spectra are strongly affected by excitons.[21]

Finally, the momentum transferred at the O K edge in the 90° scattering geometry deserves comment. Due to the near alignment of the sample crystal axes to the incident and scattered photon wave vectors, the transferred momentum of each photon is approximately 0.27 $Å^{-1}$. The mechanism of **k** selectivity in this experiment is through energy conservation, and our 0.5 eV incident photon energy resolution selects a range of momenta along each reciprocal axis that depends on the intermediate-state dispersion. Referring to the low lying unoccupied states in the band structure calculation of Sayede *et al.*,[15] the 0.5 eV photon resolution corresponds to nearly 25% of the Brillouin zone along the **b** and **c** reciprocal axes, and **k** points symmetric about the Γ point along each reciprocal axis are sampled. Photon momentum transfer broadens the range of sampled **k** points. In the worst case, **k** components from all three axes contribute, yielding a window in **k** space of approximately 50% of the **b** and **c** reciprocal axes. Along the nearly dispersionless **a** axis this broadening is immaterial. Photon momentum transfer does reduce our **k** selectivity along the strongly dispersing **b** and **c** reciprocal axes but we nevertheless observe **k** selectivity in the RIXS results.

V. CONCLUSIONS

The electronic structure of insulating α-MoO_3 has been measured using O K-edge RIXS, XES, and XAS. The results indicate that the electronic structure of α-MoO_3 is bandlike rather than completely localized. In XES spectra recorded at excitation energies well above the O K-edge absorption threshold, the entire Brillouin zone, inclusive of all O sites, is probed simultaneously. The result is a broad spectrum reflecting the total O $2p$ PDOS. In contrast, when the excitation energy is resonantly tuned to the π^* state, momentum selectivity allows the observation of states only near a symmetry point, with a suppression of weight from states nearer the edges of the Brillouin zone as a direct consequence of the band structure of α-MoO_3. Our results also indicate that the electronic structure of α-MoO_3 is highly anisotropic, and RIXS has been shown to be a useful fruitful probe of quasilow dimensionality in insulating materials.

ACKNOWLEDGMENTS

The Boston University (BU) program is supported in part by the Department of Energy under Contract No. DE-FG02-98ER45680. The ALS is supported by the U.S. Department of Energy under Contract No. DE-AC02-05CH11231. T.L. acknowledges support from the ALS. C.M. acknowledges financial support from the Irish Higher Educational Authority and Enterprise Ireland. B.K. acknowledges funding received from the Irish Research Council for Science Engineering and Technology in cooperation with INTEL Ireland. We thank Tanel Käämbre and the MAXLab staff for their assistance.

*Corresponding author; ksmith@bu.edu

[1] *Electron Spectroscopies Applied to Low-Dimensional Materials (Physics and Chemistry of Materials with Low-Dimensional Structures)*, edited by H. P. Hughes and H. Starnberg (Kluwer, Dordrecht, Netherlands, 2000); K. E. Smith, Annu. Rep. Prog. Chem., Sect. C: Phys. Chem. **90**, 115 (1993).

[2] A. L. Companion and M. Mackin, J. Chem. Phys. **42**, 4219 (1965).

[3] P. G. Dickens and D. J. Neild, Trans. Faraday Soc. **64**, 13 (1968).

[4] J. D. Denlinger, G. H. Gweon, J. W. Allen, J. Marcus, and C. Schlenker, J. Electron Spectrosc. Relat. Phenom. **101**, 805 (1999); J. D. Denlinger, G.-H. Gweon, J. W. Allen, C. G. Olson, J. Marcus, C. Schlenker, and L.-S. Hsu, Phys. Rev. Lett. **82**, 2540 (1999); A. V. Fedorov, S. A. Brazovskii, V. N. Muthukumar, P. D. Johnson, J. Xue, L. C. Duda, K. E. Smith, W. H. McCarroll, M. Greenblatt, and S. L. Hulbert, J. Phys. Condens. Matter **12**, L191 (2000); P. A. Glans, T. Learmonth, K. E. Smith, T. Valla, P. D. Johnson, S. L. Hulbert, W. McCarroll, and M. Greenblatt, Phys. Rev. B **72**, 035115 (2005); K. Breuer, K. E. Smith, M. Greenblatt, and W. McCarroll, J. Vac. Sci. Technol. A **12**, 2196 (1994); K. Breuer, D. M. Goldberg, K. E. Smith, M. Greenblatt, and W. McCarroll, Solid State Commun. **94**, 601 (1995); K. Breuer, C. Stagarescu, K. E. Smith, M. Greenblatt, and K. Ramanujachary, Phys. Rev. Lett. **76**, 3172 (1996); K. E. Smith, K. Breuer, M. Greenblatt, and W. McCarroll, *ibid.* **70**, 3772 (1993); J. Xue, L.-C. Duda, K. E. Smith, A. V. Fedorov, P. D. Johnson, S. L. Hulbert, W. H. McCarroll, and M. Greenblatt, *ibid.* **83**, 1235 (1999).

[5] J. Nordgren and N. Wassdahl, J. Electron Spectrosc. Relat. Phenom. **72**, 273 (1995); J. Nordgren, G. Bray, S. Cramm, R. Nyholm, J. E. Rubensson, and N. Wassdahl, Rev. Sci. Instrum. **60**, 1690 (1989).

[6] F. Gel'mukhanov and H. Agren, Phys. Rep. **312**, 87 (1999).

[7] Y. Ma, N. Wassdahl, P. Skytt, J. Guo, J. Nordgren, P. D. Johnson, J. E. Rubensson, T. Boske, W. Eberhardt, and S. D. Kevan, Phys. Rev. Lett. **69**, 2598 (1992).

[8] Y. Ma, Phys. Rev. B **49**, 5799 (1994).

[9] J. A. Carlisle, E. L. Shirley, E. A. Hudson, L. J. Terminello, T. A. Callcott, J. J. Jia, D. L. Ederer, R. C. C. Perera, and F. J. Himpsel, Phys. Rev. Lett. **74**, 1234 (1995).

[10] M. Greenblatt, Chem. Rev. (Washington, D.C.) **88**, 31 (1988).

[11] *Low Dimensional Electronic Properties of Molybdenum Bronzes and Oxides*, edited by C. Schlenker (Kluwer, Dordrecht, 1989).

[12] M. Sing, R. Neudert, H. von Lips, M. S. Golden, M. Knupfer, J. Fink, R. Claessen, J. Mucke, H. Schmitt, S. Hufner, B. Lommel, W. Aßmus, C. Jung, and C. Hellwig, Phys. Rev. B **60**, 8559 (1999).

[13] C. A. Rozzi, F. Manghi, and F. Parmigiani, Phys. Rev. B **68**, 075106 (2003).

[14] F. Cora, A. Patel, N. M. Harrison, C. Roetti, and C. R. A. Catlow, J. Mater. Chem. **7**, 959 (1997).

[15] A. D. Sayede, T. Amriou, M. Pernisek, B. Khelifa, and C. Mathieu, Chem. Phys. **316**, 72 (2005).

[16] J. Nordgren and R. Nyholm, Nucl. Instrum. Methods Phys. Res. A **246**, 242 (1986).

[17] F. M. F. de Groot, M. Grioni, J. C. Fuggle, J. Ghijsen, G. A. Sawatzky, and H. Petersen, Phys. Rev. B **40**, 5715 (1989).

[18] L. C. Duda, J. H. Guo, J. Nordgren, C. B. Stagarescu, K. E. Smith, W. McCarroll, K. Ramanujachary, and M. Greenblatt, Phys. Rev. B **56**, 1284 (1997).

[19] J. Stöhr, *NEXAFS Spectroscopy* (Springer, Berlin, 1992).

[20] J. A. Carlisle, S. R. Blankenship, L. J. Terminello, J. J. Jia, T. A. Callcott, D. L. Ederer, R. C. C. Perera, and F. J. Himpsel, J. Electron Spectrosc. Relat. Phenom. **110**, 323 (2000); M. van Veenendaal and P. Carra, Phys. Rev. Lett. **78**, 2839 (1997).

[21] J. F. Morar, F. J. Himpsel, G. Hollinger, G. Hughes, and J. L. Jordan, Phys. Rev. Lett. **54**, 1960 (1985).